Modulations of aerosol impacts on cloud microphysics induced by the warm Kuroshio Current under the East Asian winter monsoon

M. Koike[1*], N. Asano[1], H. Nakamura[2], S. Sakai[1], T. M. Nagao[3], and T. Y. Nakajima[4]

[1] Department of Earth and Planetary Science, Graduate School of Science, University of Tokyo, Tokyo 113-0033, Japan

[2] Research Center for Advanced Science and Technology, University of Tokyo, Tokyo 153-8904, Japan

[3] Earth Observation Research Center, Japan Aerospace Exploration Agency, 2-1-1 Sengen, Tsukuba-shi, Ibaraki 305-8505, Japan

[4] Research and Information Center, Tokai University, Tokyo 151-0063, Japan

Short title: KOIKE ET AL.: AEROSOL AND SST IMPACTS ON CLOUDS

Submitted to JGR on May 17, 2016

Revised on September 20, 2016

Authors' addresses

N. Asano, M. Koike, and S. Sakai,
Department of Earth and Planetary Science, Graduate School of Science, University of Tokyo, Hongo 7-3-1, Bunkyo-ku, Tokyo, 113-0033, Japan
(naruhiko_asano_ut@outlook.com; koike@eps.s.u-tokyo.ac.jp; sato.kakimoto@gmail.com)

T. M. Nagao,
Earth Observation Research Center, Japan Aerospace Exploration Agency, 2-1-1 Sengen, Tsukuba-shi, Ibaraki 305-8505, Japan
(nagao.takashi@jaxa.jp)

T. Y. Nakajima,
Research and Information Center, Tokai University, Tokyo 151-0063, Japan
(nkjm@yoyogi.ycc.u-tokai.ac.jp)

H. Nakamura,
Research Center for Advanced Science and Technology, University of Tokyo, 4-6-1 Komaba, Meguro-ku, Tokyo 153-8904, Japan
(hisashi@atmos.rcast.u-tokyo.ac.jp)

Key Points

1. We found that cloud droplet number concentrations are higher when surface air temperature (SST) – surface air temperature (SAT) is higher over the warm SST region.

2. The observed high cloud droplet number concentrations resulted from enhanced updraft velocities upon cold air outbreaks and high aerosol amounts.

3. The results suggest that warm SSTs affect aerosol-cloud interactions.

Abstract

In our previous aircraft observations, the possible influence of high sea surface temperature (SST) along the Kuroshio Current on aerosol-cloud interactions over the western North Pacific was revealed. The cloud droplet number concentration (N_c) was found to increase with decreasing near-surface static stability (NSS), which was evaluated locally as the difference between the SST and surface air temperature (SAT). To explore the spatial and temporal extent to which this warm SST influence can be operative, the present study analyzed N_c values estimated from Moderate Resolution Imaging Spectroradiometer (MODIS) satellite measurements. The comparison of the local N_c values between the high and low SST – SAT days revealed a marked increase in N_c (up to a factor of 1.8) along the Kuroshio Current in the southern East China Sea, where particularly high SST – SAT values (up to 8 K) were observed in winter under monsoonal cold air outflows from the Asian Continent. This cold airflow destabilizes the atmospheric boundary layer, which leads to enhanced updraft velocities within the well-developed mixed layer and thus greater N_c. The monsoonal northwesterlies also bring a large amount of anthropogenic aerosols from the Asian continent that increase N_c in the first place. These results suggest that the same modulations of cloud microphysics can occur over other warm western boundary currents, including the Gulf Stream, under polluted cool continental airflows. Possibilities of influencing the cloud liquid water path (CLWP) are also discussed.

1. Introduction

The level of uncertainty regarding the effective radiative forcing due to aerosol-cloud interactions reported in the 5th Assessment Report of the Intergovernmental Panel on Climate Change (IPCC) [*Boucher et al.*, 2013] remains comparable to that in the previous report (IPCC AR4) [*Meehl et al.*, 2007], which indicates certain difficulties in quantifying the effect. Improved quantification requires better understanding of the fundamental processes of aerosol-cloud interactions under various atmospheric/oceanic conditions. The western North Pacific is characterized by high anthropogenic aerosol emissions and thus high cloud droplet number concentrations [e.g., *Koike et al.*, 2012]. This region is also characterized by high sea-surface temperature (SST) along the Kuroshio Current (hereafter denoted by "the Kuroshio"), which is the warm western boundary current of the North Pacific subtropical oceanic gyre. This situation is in sharp contrast to the lower SST off the west coasts of North and South America, where stratocumulus clouds persistently form within the marine boundary layer (MBL), which is capped by a strong temperature inversion. The warm Kuroshio and its Extension east of Japan have recently been found to influence the MBL structure, cloud formation, and precipitation [e.g., *Xie et al.*, 2002; *Tanimoto et al.*, 2009; *Tokinaga et al.*, 2009; *Taguchi et al.*, 2009; *Xu et al.*, 2011; *Miyama et al.*, 2012; *Kawai et al.,* 2015; *Masunaga et al.,* 2015, 2016].

In our previous studies based on in-situ aircraft data, we reported that warm SST along the Kuroshio could also modulate the aerosol impacts on microphysical properties of low-altitude non-precipitating water clouds [*Koike et al.*, 2012, hereafter denoted by K12]. K12 showed that cold air outflow from the Asian continent toward the East China Sea in early spring resulted in higher cloud droplet number concentrations (N_c), especially over the Kuroshio, for the following two reasons. First, the continental airflow carries large amounts of aerosols, leading to an immediate increase in N_c; this effect was confirmed by a clear positive correlation between N_c and the accumulation-mode aerosol number concentration (N_a) below clouds. Second, the dry, cold continental airflow destabilizes the MBL, especially over the warm Kuroshio, leading to stronger updrafts and thus higher super saturations in clouds. In this situation, even small aerosols, which typically are not activated as cloud droplets in weaker updrafts, can be activated, leading to higher N_c. This mechanism was suggested by a positive correlation between the N_c/N_a ratio and the difference between the SST and the 950-hPa temperature (i.e., SST – T_{950}) defined as a measure of near-surface static stability (NSS). Cloud thickness appeared to increase over the Kuroshio under cold air outbreaks more than in other situations; we thus hypothesized that the NSS determined by both SST and large-scale airflow can modulate both aerosol impacts on cloud microphysics and the macro-structure of clouds, including the cloud base and top altitudes, and thus the cloud liquid water path (CLWP).

Cold air outbreaks from the Asian Continent toward the western Pacific frequently occur from late autumn to early spring and potentially affect cloud formation and properties over the East China Sea. In this study, we analyzed N_c values estimated from Moderate Resolution Imaging Spectroradiometer (MODIS, on board NASA's Terra satellite) measurements between 2008 and 2012 to explore the spatial and temporal extent of the warm SST mechanism mentioned above. Possible impacts on the CLWP were also examined.

In section 2, we describe the data used in this study. In section 3.1, winter averages of N_c and other related parameters are described. In sections 3.1 – 3.7, we use the difference between the SST and the surface air temperature (SAT, i.e., SST – SAT) as a measure of the NSS for comparison of N_c and other related parameters between high and low SST – SAT days. A summary is given in section 4.

2. Data

In this study, we used the N_c values estimated from the MODIS-derived cloud optical thickness (τ) and cloud effective radius (r_e) under the assumption of a vertical structure of adiabatic water clouds [*Brenguier et al.*, 2000; *Szczodrak et al.*, 2001; *Bennartz*, 2007]:

$$N_c = \alpha \cdot \tau^{0.5} \cdot r_e^{-2.5} \qquad (1)$$

where $\alpha = \left(\frac{5}{8\rho_w \pi^2}\right)^{\frac{1}{2}} \cdot k^{-1} \cdot C_w^{\frac{1}{2}}$, and ρ_w is the density of liquid water. The parameter C_w is the moist adiabatic condensate coefficient, which weakly depends on air temperature and pressure. Because C_w changes little within a thin cloud layer with a depth of less than 1 km (uncertainties in the N_c estimate would be less than 10%), C_w was calculated using the MODIS-derived cloud top temperature and pressure. The parameter k in Eq. (1) reflects the shape of the cloud-droplet size distribution, and we set k = 0.71 based on the in situ measurements in K12. For τ and r_e, we used the values retrieved from the 0.64-μm and 3.7-μm band signals (MODIS/Terra Level 1B Subsampled Calibrated Radiances, version C5) through an algorithm derived in previous studies [*Nakajima and Nakajima*, 1995; *Kawamoto et al.*, 2001; *Nakajima et al.*, 2010; *Nagao et al.*, 2013]. Because Eq. (1) was derived for adiabatic water clouds, we selected only water clouds for our analysis on the basis of the MODIS measurements (i.e., a cloud top temperature greater than 273.15 K) and only those clouds without drizzle drops ($r_{2.1}$ < 14 μm following *Nakajima et al.* [2010], where $r_{2.1}$ is the cloud effective radius retrieved from the 2.1-μm band signal). The non-precipitating water cloud selection was made for 0.1° × 0.1° averages of τ and r_e, from which N_c values were derived by Eq. (1); then, 0.75° × 0.75° averages of N_c were taken correspondingly to the spatial resolution of the meteorological data as described below. Although there are some uncertainties in the exact values of the N_c estimates, their relative variations are considered reliable [e.g., *Painemal and Zuidema*, 2011].

The MODIS-derived fine-mode aerosol optical depth (AOD) at a wavelength of 0.55 μm and 10 × 10 km^2 resolution (MOD04_L2) [*Remer et al*., 2005] was used to estimate the aerosol amount as a proxy for cloud condensation nuclei (CCN) concentrations, and the 0.75° × 0.75° averages were calculated. For the meteorological data, including SAT, wind field, and surface sensible and latent heat fluxes (SHF and LHF, respectively), the ERA-Interim global atmospheric reanalysis dataset (0.75° × 0.75°) [*Dee et al*., 2011] was used. We used 2-m air temperature data at 00UTC for the SAT. Lower-tropospheric stability (LTS), defined as the difference in the potential temperature (θ) between the 700-hPa level and the surface, was also calculated from the data. Because the temperature data are available at pressure levels at intervals of 25 hPa below the 800 hPa level, the thermal structure within the MBL is therefore well represented. The SST data compiled in the ERA-interim reanalysis dataset were also used where National Centers for Environmental Prediction (NCEP) real-time global SST (NCEP RTG) and Operational SST and sea-ice analysis (OSTIA) had been used before and after January 2009, respectively. The horizontal resolution of the SST data used for the ERA-interim reanalysis since 2002 is high enough to resolve meso-scale impacts of the fine-scale SST distribution associated with the Kuroshio and its extension on the MBL [*Masunaga et al.,* 2015, 2016].

3. Results and Discussion

3.1. Winter averages for 2009

Figure 1 shows N_c, AOD, SST, and SST – SAT averaged over the winter months in 2009 (i.e., January, February, November, and December, 2009, hereafter denoted by NDJF2009). Figure 1a shows that the N_c values (for non-precipitating water clouds) were high over the Asian Continent and systematically and gradually decreased from the coastal regions toward the Pacific. This pattern is generally considered to reflect large emission sources of aerosols and their precursor gases over the continent. In fact, the MODIS-derived fine-mode AOD also decreased offshore with increasing distance from the coast (Figure 1b). (Note that all NDJF2009 data were used for Figures 1b, 1c, and 1d, regardless of the presence/absence of clouds within 0.75° × 0.75° grid boxes). The NDJF2009 mean near-surface winds were characterized by the monsoonal winds from Asia (Figure 1d) with the northwesterlies prevailing over the ocean north of 30°N. Although not evident in this mean field, westerly winds were occasionally observed further south (approximately 25°N); these air streams efficiently brought continental air masses with high aerosol concentrations into the maritime regions.

Figure 1c shows that the SST was systematically high along the Kuroshio axis from the east of Taiwan to the east of southern Japan. The concentration of high SST into the narrow Kuroshio Current was more evident in the daily SST distributions, and the sharp SST gradient across the Kuroshio axis was slightly smoothed in the winter-mean field because of a slight displacement in the Kuroshio axis. We defined the "Kuroshio study area", indicated in Figures 1a – 1d, as a parallelogram (23°N-26°N, 122°E and 28°N-31°N, 130°E); statistical analyses were conducted for this area as described below.

Figure 1d shows that the NDJF2009 averages of SST – SAT were generally high along the Kuroshio (including the Kuroshio study area and its downstream), where the SST – SAT values exceeded 4K and locally reached as high as 7K. The SST – SAT values were also high over the continental marginal seas, including the Sea of Japan and the Yellow and East China Seas, in addition to the northern portion of the South China Sea. These high SST – SAT values were due to cold continental air outflow onto the relatively warm maritime regions. In fact, the monthly mean SST – SAT values within the Kuroshio study area were systematically higher during winter (November through February) than during any other season. Although the SST was lower in the Yellow Sea and the Sea of Japan than along the Kuroshio (Figure 1c), the SAT was sufficiently low to yield high SST – SAT values.

3.2. SST – SAT changes induced by daily meteorological conditions

Figure 2a shows a map of local differences between the highest and lowest daily SST – SAT values during NDJF2009 based only on data obtained when non-precipitating water clouds were observed locally by MODIS, hereafter denoted by Δ(SST – SAT). We stress that "Δ" signifies the differences evaluated only under non-precipitating water cloud conditions. If water clouds were observed on more than 10 days in a particular grid box (0.75° × 0.75°) within a particular month, five-day averages were calculated separately for the highest and lowest SST – SAT days and their differences were calculated. If water clouds were observed on fewer than 10 days during a given month, the corresponding averages were calculated separately for the higher and lower halves from which Δ(SST – SAT) was derived. The local four-month averages for NDJF2009 were then calculated and are shown as Δ(SST – SAT) in Figure 2a. An area of particularly high Δ(SST – SAT) was identified along the Kuroshio, and Δ(SST – SAT) values exceeded 4 K, reaching 7 K in the Kuroshio study area. The highest Δ(SST – SAT) value was observed to the north of Taiwan. These features were seen in each of the winter months in 2009, although the high Δ(SST – SAT) region as well as its amplitude varied somewhat from one month to another. These features were also seen in the winter months between 2008 and 2012, as shown in Appendix A.

Table 1 shows the SST, SAT, and SST – SAT values averaged separately for high and low SST – SAT days in NDJF2009 in the Kuroshio study area. The averages were calculated for each month; then, four-month averages were calculated. This table shows that the SST changed only slightly between the high and low SST – SAT days, which means that the high Δ(SST – SAT) values over the Kuroshio were primarily related to large SAT contrasts between the high and low SST – SAT days (ΔSAT). Figures 3a and 3b show the mean SAT and winds at 950 hPa on high and low SST – SAT days, respectively, for NDJF2009. On the high SST – SAT days (i.e., low SAT days, Figure 3a), the relatively strong northwesterlies or northerlies prevailed north of 25°N, carrying cold air mass from the continent. Because of its rather short travel time after leaving the coast, a continental air mass can preserve its coolness over the relatively cool ocean surface until reaching the warm Kuroshio. Because of this low SAT, the SST – SAT values exhibited a clear maximum over the high SST area along the Kuroshio. In contrast, calm wind conditions prevailed between 25°N and 35°N on the low SST – SAT days (i.e., high SAT days, Figure 3b). Under these conditions, an air mass, even of a continental origin, can warm up by heat exchange with the underlying ocean because of a longer exposure time, especially over the warm Kuroshio. As a result, the SST – SAT values over the Kuroshio were similar to those over other regions. Because of the contrasts between the high and low SST – SAT days, the Δ(SST – SAT) values were particularly large over the warm Kuroshio.

3.3. SST – SAT impact on N_c

Figure 2b shows fractional differences in the N_c values ($\Delta N_c/N_c$, unit: percent) of non-precipitating water clouds between the high and low SST – SAT days during NDJF2009, where the fractional differences were calculated for each of the winter months before the four-month average was taken. Monthly average N_c values in individual grid boxes were used for the denominator of $\Delta N_c/N_c$. Areas with high $\Delta N_c/N_c$ values generally correspond to high Δ(SST – SAT) areas along the Kuroshio in the southern portion of the East China Sea. In our Kuroshio study area, the N_c values calculated on the high SST – SAT days were 30~80% greater than on the low SST – SAT days ($\Delta N_c/N_c$ = 38%, on average, as shown in Table 2). In addition to the Kuroshio area, both ΔN_c and Δ(SST – SAT) tended to be high off the southern coast of China in the northern part of the South China Sea. These features were also recognized in other winter months between 2008 and 2012 (Appendix A). Moreover, these features were also evident when the slope of the linear regression line $(dN_c/N_c)/d(SST–SAT))$ was calculated instead of $\Delta N_c/N_c$ values (Appendix B), suggesting the robustness of the present analyses.

Because the N_c values were estimated from MODIS-derived cloud optical thickness (τ) and cloud effective radius (r_e) using Eq. (1) (section 2), the contribution from each of the two parameters ($\Delta N_c/N_c = 0.5\Delta\tau/\tau - 2.5\Delta r_e/r_e$) was assessed in Figures 2c and 2d. The contributions from τ ($0.5\Delta\tau/\tau$) and r_e ($-2.5\Delta r_e/r_e$) were generally positive between 20°N and 28°N; thus both the parameters contributed to the increase in $\Delta N_c/N_c$ values in the study area. In fact, Table 2 shows that, on average in the Kuroshio study area, $0.5\Delta\tau/\tau$ and $-2.5\Delta r_e/r_e$ values were 17 and 28%, respectively, suggesting that the contributions of these two parameters to $\Delta N_c/N_c$ were comparable. Nevertheless, their relative importance tended to exhibit an apparent latitudinal dependence. The contribution from r_e was generally positive and dominant over the East China and Yellow Seas (Figure 2d). Contrastingly, the contribution from τ was dominantly positive over the South China Sea and to the east of Taiwan (Figure 2c), however it was negative over the cooler regions, including the Yellow Sea and the northern portion of the East China Sea (Figure 2c). The latter features corresponded to negative ΔCLWP/CLWP values over these regions, which were likely due to a reduction in the total water amount in cold air as described later in section 3.6.

As discussed in K12, the high ΔN_c area along the Kuroshio in winter is likely due to a combination of two factors. First, a cold, dry air mass originating from the continent destabilized the atmospheric boundary layer over the warm Kuroshio, thus yielding greater updraft velocities and hence greater N_c. Second, the continental air mass brought large amounts of anthropogenic aerosols, which increased N_c. In fact, ΔAOD (differences in the AOD between the high and low SST – SAT days for NDJF2009) was generally positive south of 28°N (Figure 2e). Additionally, the low temperatures of the continental air mass also influenced cloud formation to some extent due to the temperature dependence of the saturation vapor pressure represented in the Clausius – Clapeyron equation, as described in Appendix C.

To evaluate the impacts of aerosols and SST – SAT separately, the averaged N_c values in the Kuroshio study area are shown separately for various ranges of SST – SAT and AOD, on the basis of their daily 0.75° × 0.75° data during NDJF2009 (Figure 4). This figure shows that the N_c values generally increased with AOD. In each of the AOD ranges, the N_c values also tended to increase with increasing SST – SAT, which is consistent with the impact of NSS on updraft velocities. The N_c values increased by 40 – 80% with an 8 K increase in SST – SAT; this sensitivity was generally higher (with a steeper slope in Figure 4) for higher AOD values. Moreover, the ratio of N_c between low and high AODs (N_c(highAOD)/N_c(lowAOD)) was generally higher for greater SST – SAT values; the ratio increased by a factor of 1.5 (at most) for high SST – SAT conditions (9 K) compared with low conditions (1 K). Impacts of aerosols on N_c thus tend to be enhanced under the conditions of higher SST – SAT, indicative of possible influences of SST on aerosol – cloud interactions.

The results presented above are overall consistent with the in-situ measurements and cloud parcel model calculations presented in K12, which showed that a 12 K increase in the SST – T_{950} resulted in nearly doubled aircraft-derived N_c values if normalized by the accumulation-mode aerosol number concentrations (N_a). Through their air parcel model calculations (Figure 10 in K12), K12 also showed that the aerosol impacts on N_c tended to be enhanced under higher updraft velocities (w); the ratio N_c(high_N_a)/N_c(low_N_a) was higher by a factor of 1.6 when w = 120 cm s^{-1} (corresponding to high SST – SAT) than when w = 40 cm s^{-1} (corresponding to low SST – SAT). Under the low N_a conditions examined in K12, a large fraction of aerosols was activated even under low updraft velocity, and an increase in the updraft velocity therefore yielded only a small fractional increase in N_c compared with the high N_a conditions.

We evaluated the relative contributions of SST – SAT and AOD to N_c variations within the Kuroshio study area during NDJF2009. Although $\partial N_c/\partial(\mathrm{AOD})$ depends on SST – SAT (and vice versa), we ignored cross-correlation terms and simply calculated the linear regression coefficients between N_c and SST – SAT (for individual AOD ranges) and between N_c and AOD (for individual SST – SAT ranges). Thus, the regression coefficients simply correspond to partial derivatives, and $\partial N_c/\partial(\mathrm{AOD}) = 320$ $\mathrm{cm^{-3}}$ and $\partial N_c/\partial(\mathrm{SST} - \mathrm{SAT}) = 18.8\ \mathrm{cm^{-3}\ K^{-1}}$ were obtained. Evaluations of the standard deviations of AOD and SST – SAT within the Kuroshio study area during NDJF2009 thus led to the estimates of 40 and 52 $\mathrm{cm^{-3}}$ for the standard deviations of N_c caused solely by changes in AOD and SST – SAT, respectively ($\sigma_{Nc} = \partial N_c/\partial(\mathrm{AOD})\ \sigma_{AOD}$ and $\sigma_{Nc} = \partial N_c/\partial(\mathrm{SST{-}SAT})\ \sigma_{SST\text{-}SAT}$). This result suggests that the destabilization effect under cold air advection over the warm Kuroshio water plays a comparable or even more important role in N_c variability than AOD changes. Thus, high N_c values observed in the day-to-day variations over the East China Sea were not only due to aerosol transport but also due to the presence of high SST, a distinctive characteristic of the western Pacific.

In order to confirm the importance of NSS, we repeated the same evaluations as above but for summer months of 2009, in which SST – SAT on average diminished in our study area and its day-to-day variations were smaller than in the winter months. As a consequence, N_c changes in association with SST – SAT changes were not evident (not shown). The SST impacts on aerosol – cloud interaction are expected to be prevalent for geographical locations and seasons where SST – SAT becomes strongly positive under cold-air outbreaks.

3.4. Correlation between SST – SAT and AOD

The $\Delta N_c/N_c$ values were rather low along the Kuroshio off the southern coast of Japan (approximately 30°N and 130 – 135°E, Figure 2b) despite high Δ(SST – SAT) values (Figure 2a). In this region, the ΔAOD/AOD values were negative (Figure 2e), suggesting that the effects of greater updrafts due to high SST – SAT values under the northwesterly conditions tend to be offset by lower aerosol concentrations (low AOD), thus leading to low ΔN_c values. In fact, the correlation coefficients between SST – SAT and AOD were negative at latitudes north of 28°N (Figure 2f).

The lower aerosol concentrations associated with the northwesterlies on high SST – SAT days resulted possibly from the transport of relatively clean air originating from the area north of 40°N, where anthropogenic emissions are relatively low [e.g., *Streets et al.*, 2003]. Some of the aerosols being transported might also have been removed by precipitation that tends to be organized under the cold-air outbreaks over the Sea of Japan and the Yellow Sea, as can be confirmed by the ERA-Interim re-analysis (not shown). On low SST – SAT days, by contrast, polluted air, possibly of local origin, may have stagnated off the southern coast of Japan under the calm wind conditions, leading to the negative ΔAOD values in this region.

3.5. Boundary layer structure and surface heat fluxes

Figure 5 shows the vertical profiles of the potential temperature separately averaged within the Kuroshio study area for the high and low SST – SAT days based on the ERA-Interim. The arrow shows the average SST, which differed only slightly between the high and low SST – SAT days (0.02 K, Table 1). The average potential temperature profile for the high SST – SAT days is almost vertically uniform below the 900-hPa level (approximately 1 km), which indicates enhanced vertical mixing within the well-developed unstable mixed layer under the unstable NSS condition. In contrast, the MBL was more stable on the low SST – SAT days, which led to less efficient vertical mixing and therefore a much shallower mixed layer. These results are consistent with our hypothesis that high SST – SAT destabilized the lower troposphere, giving rise to stronger vertical motion within the well-developed mixed layer.

Figure 6a shows the local differences in the mean SHF between the high and low SST – SAT days (ΔSHF) based on the ERA-Interim dataset for NDJF2009. Similar to the other Δ values, the ΔSHF values were only based on the data when and where non-precipitating water clouds were observed. The spatial distribution of ΔSHF was similar to that of Δ(SST – SAT); its high values (80 – 120 W m^{-2}) were near the Kuroshio primarily because SHF is approximately proportional to SST – SAT. Additionally, SHF is proportional to surface wind speed, which tends be greater under high SST – SAT conditions due to enhanced vertical mixing of wind momentum [e.g., *Wallace et al.*, 1989; *Tokinaga et al.*, 2009]. At the same time, the enhanced SHF acted to destabilized the MBL, contributing to the enhancement of the turbulent mixing and thus the development of the mixed layer.

Figure 6b shows that the mean local LHF differences between the high and low SST – SAT days (ΔLHF) for NDJF2009 were also particularly large (160 – 280 W m^{-2}, with a Bowen ratio ΔSHF/ΔLHF of 0.4 – 0.5) over the warm Kuroshio. The LHF is proportional to the air-sea moisture difference, in which high SST has a positive contribution. Because of the strong temperature dependence of the saturated specific humidity, the LHF tends to be particularly large over the Kuroshio, especially under outbreaks of cold, dry continental air. With the abundant moisture supply from the warm Kuroshio, enhanced latent heat release during cloud formation can strengthen uplifting at the cloud base. Although a quantification of the relative importance of the contributions from the SHF and LHF is beyond the scope of the present study, warm SST enhances the turbulent heat fluxes, which can contribute to the formation of a well-mixed boundary layer and strong updrafts.

3.6. Changes in cloud liquid water path

Cloud liquid water path (CLWP) can be estimated by assuming a vertical structure of adiabatic water clouds [*Brenguier et al.*, 2000; *Szczodrak et al.*, 2001; *Bennartz*, 2007]:

$$CLWP = \frac{5\rho_w}{9} \cdot \tau \cdot r_e \qquad (2)$$

where ρ_w is the density of liquid water. Using the same MODIS data set used for estimating N_c for non-precipitating water clouds, the corresponding winter averages (NDJF2009) of CLWP and ΔCLWP/CLWP (the differences between high and low SST – SAT days normalized by averages) were estimated (Figures 7a and 7b, respectively). Figure 7a shows that the CLWP over the ocean was generally greater over the southern portion of the East China Sea. Markedly high CLWP values exceeding 70 g m^{-2} were seen in northeast of Taiwan along the Kuroshio (the Kuroshio study area). This geographical tendency is consistent with previous studies based on satellite-based microwave observations [e.g., *O'Dell et al.*, 2008]. Their estimation of CLWP values, however reached as much as 150 to 250 g m^{-2} over the Kuroshio, which is twice to three times greater than our estimation. This discrepancy is likely because only non-precipitating clouds were selected in our estimation.

Figure 7b shows that the spatial distribution of the ΔCLWP/CLWP values was generally similar to that of $\Delta\tau/\tau$ (Figure 2c) and ΔAOD/AOD (Figure 2e), and they were relatively high over the Kuroshio study area. Table 1 shows that the average CLWP was greater by 41% on high SST – SAT days compared with values on low SST – SAT days, although the standard deviations were large.

Figure 7c shows a scatter plot between CLWP and SST – SAT using all 0.75° × 0.75° data (non-precipitating water clouds) obtained within the Kuroshio study area during NDJF2009. Overall no clear correlation was found between the two parameters, except a slight tendency for the CLWP values to increase with increasing SST – SAT (the black line, for SST – SAT < 8 K). This tendency arose mostly from data, in which the CLWP exceeded 80 g m^{-2} (red line), where a 40% increase was found in association with an increase in SST – SAT of 8 K. Although not shown here, no clear dependence on AOD was found in these tendencies: quite similar tendencies were found when the data in different AOD ranges were examined (as was done for N_c, shown in Figure 4).

The mechanisms for inducing the observed slight CLWP increase with increasing SST – SAT are not understood. The CLWP can be affected by the large-scale meteorological conditions as well as various cloud dynamical/microphysical processes. For example, negative ΔCLWP values north of 30°N are likely due to a reduction in the total water amount in cold air mass (as expected from the Clausius –

Clapeyron equation). The cold air outbreak can also affect the CLWP through modifying the MBL structure. Although analyses of satellite data suggested that aerosols could affect the CLWP [e.g., *Lebsock et al*., 2008; *Quaas et al*., 2008; *Chen et al*., 2014], these influences are considered to depend on large-scale meteorological conditions and aerosol loading. It is beyond the scope of this study to examine SST impacts on the CLWP and aerosol–CLWP relationship under different meteorological conditions, and further analyses focusing on these parameters should be performed in the future.

3.7. Relationship with lower-tropospheric stability

Lower-tropospheric stability (LTS), defined as the difference in the potential temperature (θ) between the 700-hPa level and the surface [*Klein and Hartmann*, 1993], has been widely used as a measure of the temperature inversion strength for investigating relationships with low-level cloud parameters [e.g., *Wood and Bretherton*, 2006]. The NSS (evaluated by SST – SAT) introduced in this study is a possible measure of turbulence activity in the boundary layer, whereas the LTS is a possible measure of trapping strength of moist air that may lead to an increase in cloudiness. Using the global satellite observations of clouds from the Tropical Rainfall Measuring Mission (TRMM), *Matsui et al*. [2006] showed that the cloud droplet effective radius (r_e) is negatively correlated with the LTS over most of the globe, although the underlying mechanisms were not discussed. Under a fixed cloud liquid water content, smaller r_e values correspond to higher N_c values. Therefore, the results of *Matsui et al*. [2006] suggest a positive correlation between N_c and LTS.

Figure 8 shows the mean local LTS differences between the high and low SST

– SAT days (ΔLTS), calculated using the ERA-Interim data for NDJF2009 only under non-precipitating water cloud conditions. Within the Kuroshio study area, a positive signal (0 – 4 K) was found, indicative of a positive correlation with N_c (c.f., Figure 2b). Even higher ΔLTS values (3 – 5 K) were found just off the central coast of China, a region slightly to the west of the Kuroshio study area, and off the southern coast of China. The positive ΔLTS values in these regions were likely to occur because cold air advection near the surface on high SST – SAT days tends to decrease the potential temperature more at the surface than at the 700-hPa level (Figure 5) under increased mid-tropospheric subsidence, leading to an increase in LTS. The decreasing positive ΔLTS values away from the coast probably were due to warming of the continental airflow by increased heat release (ΔSHF > 0) from the sea surface (Figure 6a). Consequently, both the higher N_c and LTS values near the Kuroshio in the East China Sea were induced by the cold northwesterlies, although their positive correlation indicates no cause-and-effect relationship between the two parameters.

Except for the continental marginal seas described above (the Kuroshio study area and coastal regions), ΔLTS values were generally positive and negative at latitudes south and north of 27°N, respectively. The regions of negative ΔLTS values to the south of Japan generally corresponded to those of negative $\Delta N_c/N_c$ values (Figure 2b), which is also indicative of a positive correlation between those two parameters (LTS and N_c). As described in section 3.4, the negative $\Delta N_c/N_c$ values were likely related to the transport of clean air, whereas the negative ΔLTS values were likely due to cold air transport that extended above the 700 hPa level and surface heating by the warm Kuroshio. Again, this positive correlation indicates no cause-and-effect relationship.

There may be several other mechanisms that could yield some correlation between N_c and LTS (or r_e and LTS) over the globe, especially if precipitating clouds are included in the analyses. For non-precipitating clouds, N_c is primarily controlled by the aerosol number concentration, updraft velocity, and entrainment/evaporation. The mechanisms presented here are two of the possible mechanisms for the findings obtained from in global satellite observations.

4. Summary

In the present study the MODIS-derived cloud droplet number concentration (N_c) is analyzed to identify the impacts of the warm Kuroshio Current on the aerosol-cloud interaction that was suggested by our previous aircraft measurements (K12). For non-precipitating water clouds, the N_c difference between high and low SST – SAT days ($\Delta N_c/N_c$) in winter (January, February, November, and December 2009) is found to be systematically larger around the Kuroshio in the East China Sea than over other maritime areas in the western North Pacific. This enhancement in $\Delta N_c/N_c$ around the Kuroshio is also observed in statistics for five winters between 2008 and 2012, although the degree of the enhancement varies from one winter to another depending on the strength of the cold monsoonal northwesterlies.

The $\Delta N_c/N_c$ enhancement over the Kuroshio is likely explained by the two factors that were proposed in our previous study (K12). First, the northwesterly winds bring large amounts of aerosols from the continent, leading to an immediate increase in N_c. Second, those outbreaks of cold continental air mass result in destabilization of the MBL, leading to large uplifting velocities with more vigorous MBL turbulence and therefore a greater super-saturation level in the uplifted air parcels and thereby a further increase in N_c. These two mechanisms have been recognized as the positive correlations between N_c and AOD and between N_c and SST – SAT. Over the warm Kuroshio in the East China Sea, enhancement in N_c by a factor of 1.4 to 1.8 is observed in association with an increase of SST – SAT up to 8 K. Furthermore, the ratio N_c(highAOD)/N_c(lowAOD) tends to be higher under greater SST – SAT conditions, suggesting a tendency for the aerosol impacts on cloud droplet number concentration to be greater under higher SST conditions. Comparison of the relative contributions between SST – SAT and AOD to N_c variations around the Kuroshio in the East China Sea indicates that the destabilization effect under cold air advection plays a comparable or even greater role in the N_c variabilities.

The particularly large Δ(SST – SAT) values observed around the Kuroshio in the East China Sea (relative to other areas) are mostly due to large ΔSAT values between high and low SST – SAT days. On high SST – SAT (i.e., low SAT) days, a cold, dry continental air mass is transported toward the warm Kuroshio within a short time period (approximately one day) with small increase in SAT, leading to systematically high SST – SAT over the Kuroshio. In contrast, on low SST – SAT (i.e., high SAT) days, the SST – SAT values are comparable between the Kuroshio and other areas under the calm condition, resulting in thermal adjustments of SAT more closely toward SST.

On the high SST – SAT days, the mixed layer tends to well develop over the warm Kuroshio under the cold air advection near the surface. The ΔSHF and ΔLHF reached 80 – 120 and 160 – 280 W m^{-2}, respectively, and both the heat and moisture fluxes likely contributed to the mixed-layer development and enhanced uplifting of moist air mass at the cloud base, leading to higher N_c. The CLWP values are also higher over the Kuroshio and they appear to increase slightly with SST – SAT (positive ΔCLWP) especially when CLWP > 80 g m^{-3}. However, SST impacts on CLWP as well as aerosol-CLWP relationship are not conclusive in this study, because CLWP can be affected by various meteorological parameters/processes.

The aforementioned impacts of the warm SST on cloud microphysics over the western Pacific revealed in this study can potentially be operative in other maritime areas where SST – SAT becomes strongly positive under polluted continental airflow, such as around the Gulf Stream in the North Atlantic. As the next step, quantitative evaluations of the mechanisms described in this study should be conducted using numerical model calculations.

Appendix A

To substantiate the findings of the impacts of SST on cloud microphysics derived from the single-year data (NDJF2009), here we present the corresponding statistics for five winters between 2008 and 2012 (denoted by NDJF 2008-2012). Figures A1a – A1c are the same as Figures 2a, 2b, and 2e (Δ(SST – SAT), $\Delta N_c/N_c$, and ΔAOD/AOD) but for the NDJF 2008-2012 data. As in the NDJF2009 analyses, the differences were first calculated for individual winter months before taking the 20-month averages. The overall similarities are obvious between the statistics based on the 2009 data and the five-year data. Both Δ(SST – SAT) and $\Delta N_c/N_c$ maximize to the northeast of Taiwan around the Kuroshio, although the peak values are reduced in the five-winter average because of year-to-year variations in the precise locations of the maxima.

Figure A1d is the same as Figure 4 but for the NDJF 2008-2012 data. The N_c values generally increase with increasing both SST – SAT and AOD, as seen in the NDJF2009 data. Obviously, the regional impacts of the warm Kuroshio on cloud microphysics are observed every winter.

Appendix B

In previous studies, aerosol impacts on cloud microphysics were generally evaluated by taking partial derivative (a slope of a linear regression line derived using all data) of two quantities (e.g., $d \ln N_c$ / $d \ln AOD$, *Feingold et al*., 2001; *Chen et al*., 2014), whereas differences between two subsets ($\Delta N_c/N_c$ between high and low SST – SAT days) were evaluated in this study. To verify the consistency between these two methods, a normalized slope of a regression line between N_c and SST–SAT, $(dN_c/\langle N_c \rangle)/d(SST–SAT)$, was calculated for individual 0.75° × 0.75° grid boxes by using all daily data during NDJF2009 (non-precipitating water clouds). $\langle N_c \rangle$ is the four-month average in individual grid boxes. Figure B1a shows the slopes (% K^{-1}), whereas Figure B1b shows the slopes multiplied by $\Delta(SST–SAT)$, namely, $[(dN_c/\langle N_c \rangle)/d(SST–SAT)]\ \Delta(SST–SAT)$ (%), where $\Delta(SST–SAT)$ is the difference in SST–SAT between high and low SST–SAT days shown in Figure 2a. Figure B1b shows that the spatial pattern of $[(dN_c/\langle N_c \rangle)/d(SST–SAT)]\ \Delta(SST–SAT)$ values was overall similar to that of $\Delta N_c/N_c$ shown in Figure 2b. High values were located along the Kuroshio in the southern portion of the East China Sea (to the northeast of Taiwan) and off the southern coast of China (approximately 20°N and 110 – 120°E). This result indicates that the methods adopted in this study are generally consistent with those in previous studies, and the results presented in this study using ΔN_c are robust.

Figure B1a shows that the slope, $(dN_c/\langle N_c \rangle)/d(SST–SAT)$, is generally high over the Kuroshio, however this feature is less pronounced compared with that around 20°N. This result indicates that high $\Delta(SST–SAT)$ values over the Kuroshio contributed to the high $[(dN_c/\langle N_c \rangle)/d(SST–SAT)]\ \Delta(SST–SAT)$ values in that region.

The higher $(dN_c/\langle N_c\rangle)/d(SST–SAT)$ values around 20°N were likely due to higher AOD values on high SST–SAT days as shown in Figure 2e.

Likewise, Figure B1c shows the spatial pattern of $[(dAOD/\langle AOD\rangle)/d(SST–SAT)]\ \Delta(SST–SAT)$ (%) values, which was again overall similar to that of ΔAOD/AOD shown in Figure 2e. This result also suggests the robustness of the results presented in this study. The increase in the Kuroshio study area was less pronounced for $(dAOD/\langle AOD\rangle)/d(SST–SAT)$ values as for N_c.

Appendix C

Because of the temperature dependence of water saturation vapor pressure (the Clausius – Clapeyron equation), the low temperature of outflow from the continent affects the supersaturation level at the cloud base. Curvature effect on equilibrium vapor pressure of water droplet also depends slightly on temperature. These air temperature effects were evaluated by using the cloud parcel model (box model) described by *Feingold and Heymsfield* [1992], which was also used by K12. We used an aerosol size distribution (shown in Figure 10a in K12) as typical for polluted air. Vertical velocity was fixed as 80 cm s^{-1}, as typically observed upon cold air outbreaks (K12). Calculations were conducted for various initial values of 950-hPa temperature between 4 and 20°C, covering SAT variations around the Kuroshio study area.

The model experiment shows that the maximum supersaturation of an uplifted air parcel tends to increase with decreasing initial near-surface temperature and thus N_c tends to increase for a given aerosol number density. Because ΔSAT was 5 – 7K in the Kuroshio study area for NDJF2009, this temperature effect can increase N_c by 6 – 9% between high and low SST – SAT days. As described in Section 3.3, ΔN_c values are 30 – 80% of N_c values (Figure 2b) and more than half of this is due to the SST – SAT effect (the rest was due to the aerosol effect). On the basis of these facts, the air temperature effects may be approximately 20% of the SST – SAT effect.

Acknowledgments

We thank Mrs. Ikuyo Oshima for her contributions to the data analyses. This study was supported by the Ministry of Education, Culture, Sports, Science, and Technology (MEXT) in Japan (Grant-in-Aid for Scientific Research (A) 26241003, Grant-in-Aid for Scientific Research on Innovative Areas 25106706, 2205, and 2409, the GRENE Arctic Climate Change Research Project, and ArCS Project). This study was also supported by the global environment research funds from the Japanese Ministry of the Environment 2-1403 and 2-1503 and the JAXA EarthCARE project. The MODIS 3.7-μm products used in this study were retrieved from the MODIS/Terra Level 1B Subsampled Calibrated Radiances, version C5 data, which are available from http://ladsweb.nascom.nasa.gov. The cloud products from MODIS 3.7-μm data are available from the authors upon request. The MODIS AOD data are available from http://ladsweb.nascom.nasa.gov. The SST, SAT, SHF, LHF, and wind used data are the ERA-Interim global atmospheric re-analysis data, which are available from http://data-portal.ecmwf.int/data/d/interim_full_daily/.

References

Bennartz, R. (2007), Global assessment of marine boundary layer cloud droplet number concentration from satellite, *J. Geophys. Res., 112*, D02201, doi:10.1029/2006JD007547.

Boucher, O., et al. (2013), Climate Change 2013: The Physical Science Basis. Contribution of Working Group I to the Fourth Assessment Report of the Intergovernmental Panel on Climate Change (Cambridge Univ. Press, Cambridge, U. K.).

Brenguier, J. L., H. Pawlowska, L. Schuller, R. Preusker, J. Fischer, and Y. Fouquart (2000), Radiative properties of boundary layer clouds: Droplet effective radius versus number concentration, *Bull. Am. Meteorol. Soc., 57*, 803-821.

Chen, Y.-C., M. W. Christensen, G. L. Stephens, and J. H. Seinfeld (2014), Satellite-based estimate of global aerosol-cloud radiative forcing by marine warm clouds, *Nature Geosci, 7 (8)*, 643-646, doi:10.1038/ngeo2214.

Dee, D. P., et al. (2011), The ERA-Interim reanalysis: configuration and performance of the data assimilation system, *Q. J. Roy. Meteorol. Soc., 137*, 553-597.

Feingold, G., and A. J. Heymsfield (1992), Parameterizations of condensational growth of droplets for use in general circulation models, *J. Amots. Sci*., *49*, 2325-2342.

Feingold, G., L. A. Remer, J. Ramaprasad, and Y. J. Kaufman (2001), Analysis of smoke impact on clouds in Brazilian biomass burning regions: An extension of Twomey's approach, *J. Geophys. Res., 106*, 22,907– 22,922.

Kawai, Y., T. Miyama, S. Iizuka, A. Manda, M. K. Yoshioka, S. Katagiri, Y. Tachibana, and H. Nakamura (2015), Marine atmospheric boundary layer and low-level cloud responses to the Kuroshio Extension front in the early summer of 2012: three‑vessel simultaneous observations and numerical simulations, *J. Oceanogr, 71*, 511-526.

Kawamoto, K., T. Nakajima, and T. Y. Nakajima (2001), A global determination of cloud microphysics with AVHRR remote sensing, *J. Clim., 14*, 2054-2068.

Klein, S. A., and D. L. Hartmann (1993), The seasonal cycle of low stratiform clouds. *J. Clim., 6***,** 1588–1606.

Koike, M., N. Takegawa, N. Moteki, Y. Kondo, H. Nakamura, K. Kita, H. Matsui, N. Oshima, M. Kajino, and T. Y. Nakajima (2012), Measurements of Regional-Scale Aerosol Impacts on Cloud Microphysics over the East China Sea: Possible Influences of Warm Sea Surface Temperature over the Kuroshio Ocean Current, *J. Geophys. Res., 117*, D17205, doi:10.1029/2011JD017324.

Lebsock, M. D., G. L. Stephens, and C. Kummerow (2008), Multisensor satellite observations of aerosol effects on warm clouds, *J. Geophys. Res., 113*, D15,205, doi:10.1029/2008JD009876.

Masunaga, R., H. Nakamura, T. Miyasaka, K. Nishii, and Y. Tanimoto (2015), Separation of climatological imprints of the Kuroshio Extension and Oyashio fronts on the wintertime atmospheric boundary layer: Their sensitivity to SST resolution prescribed for atmospheric reanalysis, *J. Clim., 28***,** 1764–1787.

Masunaga, R., H. Nakamura, T. Miyasaka, K. Nishii, and B. Qiu (2016), Interannual modulations of oceanic imprints on the wintertime atmospheric boundary layer under the changing dynamical regimes of the Kuroshio Extension, *J. Clim., 29***,** 3273–3296.

Matsui, T., H. Masunaga, S. M. Kreidenweis, R. A. Pielke Sr., W.-K. Tao, M. Chin, and Y. J. Kaufman (2006), Satellite-based assessment of marine low cloud variability associated with aerosol, atmospheric stability, and the diurnal cycle, *J. Geophys. Res., 111,* D17204, doi:10.1029/2005JD006097.

Meehl, G. A., C. Covey, T. Delworth, M. Latif, B. McAvaney, J. F. B. Mitchell, R. J. Stouffer, and K. E. Taylor, 2007: The WCRP CMIP3 multi-model dataset: A new era in climate change research, *Bull. Am. Meteorol. Soc.*, *88, 1383–1394*.

Miyama, T., M. Nonaka, H. Nakamura, and A. Kuwano-Yoshida (2012), A striking early-sumer event of a convective rainband persistent along the warm Kuroshio in the East China Sea, *Tellus A 2012, 64*, 18962.

Nagao, T., K. Suzuki, and T. Y. Nakajima (2013), Interpretation of multiwavelength-retrieved droplet effective radii for warm water clouds in terms of in-cloud vertical inhomogeneity by using spectral bin microphysics cloud model, *J. Atmos. Sci., 70*, 2367-2392.

Nakajima, T. Y., and T. Nakajima (1995), Wide-area determination of cloud microphysical properties from NOAA ANHRR measurements for FIRE and ASTEX regions, *J. Atmos. Sci., 52*, 4043-4059.

Nakajima, T. Y., K. Suzuki, and G. L. Stephens (2010), Droplet growth in warm water clouds observed by the A-Train. Part I: Sensitivity analysis of the MODIS-derived cloud droplet size, *J. Atmos. Sci., 67*, 1884-1896.

O’Dell, C. W., F. J. Wentz, and R. Bennartz (2008), Cloud liquid water path from satellite-based passive microwave observations: A new climatology over the global ocean, *J. Clim., 21*, 1721-1739.

Painemal, D., and P. Zuidema (2011), Assessment of MODIS cloud effective radius and optical thickness retrievals over the Southeast Pacific with VOCALS-Rex in situ measurements, *J. Geophys. Res., 116*, D24206, doi:10.1029/2011JD016155.

Quaas, J., O. Boucher, N. Bellouin, and S. Kinne (2008), Satellite-based estimate of the direct and indirect aerosol climate forcing, *J. Geophys. Res., 113*, D05,204, doi:10.1029/2007JD008962.

Remer, L. A., et al. (2005), The MODIS aerosol algorithm, products, and validation, *J. Atmos. Sci., 62*, 947– 973, doi:10.1175/JAS3385.1.

Streets, D. G., et al. (2003), An inventory of gaseous and primary aerosol emissions in Asia in the year 2000, *J. Geophys. Res., 108(D21),* 8809, doi:10.1029/2002JD003093, 2003.

Szczodrak, M., Austin, P. H., and Krummel, P. B. (2001), Variability of optical depth and effective radius in marine stratocumulus clouds, *J. Atmos. Sci., 58,* 2912–2926.

Taguchi, B., H. Nakamura, M. Nonaka, and S.-P. Xie (2009), Influence of the Kuroshio/Oyashio Extensions on air-sea heat exchanges and storm-track activity as revealed in regional atmospheric model simulations for the 2003/04 cold season, *J. Clim., 22*, 6536-6560.

Tanimoto, Y., S.-P. Xie, K. Kai, H. Okajima, H. Tokinaga, T. Murayama, M. Nonaka, and H. Nakamura (2009), Observations of marine atmospheric boundary layer transitions across the summer Kuroshio Extension, *J. Clim., 22*, 1360-1374.

Tokinaga, H., Y. Tanimoto, S.-P. Xie, T. Sampe, H. Tomita, and H. Ichikawa (2009), Ocean frontal effects on the vertical development of clouds over the Western North Pacific: In situ and satellite observations, *J. Clim., 22*, 4241-4260.

Wallace, J. M., T. P. Mitchell, and C. Deser (1989), The influence of sea-surface temperature on surface wind in the Eastern Equatorial Pacific: Seasonal and interannual variability, *J. Clim., 2*, 1492-1499.

Wood, R., and C. S. Bretherton (2006), On the relationship between stratiform low cloud cover and lower-tropospheric stability, *J. Clim., 19*, 6425-6432.

Xie, S.-P., J. Hafner, Y. Tanimoto, W. T. Liu, H. Tokinaga, and H. Xu (2002), Bathymetric effect on the winter sea surface temperature and climate of the Yellow and East China Seas, *Geophys. Res. Lett., 29*, doi:10.1029/2002GL015884.

Xu, H., M. Xu, S.-P. Xie, Y. Wang (2011), Deep atmospheric response to the spring Kuroshio over the East China Sea, *J. Clim., 24*, 4959-4972.

Figure Captions

Figure 1. Winter averages in 2009 (January, February, November, and December 2009, denoted by NDJF2009): (a) MODIS-derived cloud droplet number concentration, N_c, for non-precipitating water clouds based on Eq. (1); (b) MODIS-derived fine-mode aerosol optical depth (AOD); (c) Sea surface temperature (SST); (d) SST – SAT, where SAT is surface air temperature. Time-mean 950-hPa winds are superimposed. For Figures 1b, 1c, and 1d, all data are used, irrespective of presence/absence of clouds within 0.75° × 0.75° grid boxes. The parallelogram domain (23°N-26°N, 122°E and 28°N-31°N, 130°E) shown in each panel indicates the "Kuroshio study area" defined in this study, for which the detailed statistical analyses are carried out (Tables 1 and 2).

Figure 2. (a) Local differences between the high and low daily SST – SAT values in NDJF2009 (denoted as Δ(SST – SAT)), based only on data obtained when non-precipitating water clouds were observed locally by MODIS. Monthly averages had been calculated first before four-month averages were taken. (b) Fractional differences in N_c values ($\Delta N_c/N_c$) for non-precipitating water clouds between the high and low SST – SAT days in NDJF2009. (c) Same as (b) but for the contribution from the cloud optical thickness τ to $\Delta N_c/N_c$ ($0.5\ \Delta\tau/\tau$ because of the τ dependence of N_c given in eq. (1)). (d) Same as (b) but for the contribution from the cloud effective radius r_e to $\Delta N_c/N_c$ ($-2.5\ \Delta r_e/r_e$ because of the r_e dependence of N_c given in eq. (1)). (e) Difference in fine-mode AOD (ΔAOD/AOD) between the high and low SST – SAT days in NDJF2009. (d) Local correlation coefficient between daily values of SST – SAT and AOD in

NDJF2009.

Figure 3. SAT and 950-hPa wind on (a) high and (b) low SST – SAT days in NDFJ2009. Monthly averages had been calculated first before four-month averages were taken.

Figure 4. Relationship between N_c and SST – SAT for individual AOD ranges based on daily 0.75° × 0.75° data in the "Kuroshio study area" (parallelogram area shown in Figures 1 - 3) in NDJF2009. Averages are shown where more than 10 samples are available. Total numbers of samples for AOD ranges <0.1, 0.1-0.15, 0.15-0.2, 0.2-0.3, 0.3-0.5, and >0.5 are 353, 353, 330, 290, 203, and 34, respectively, while total numbers of samples for SST – SAT ranges 0-2, 2-4, 4-6, 6-8, 8-10 K are 208, 432, 382, 257, and 153, respectively. Vertical bars indicate standard deviations divided by the square root of the sample numbers, corresponding to standard deviations of estimated averages.

Figure 5. Vertical profiles of potential temperature in the Kuroshio study area averaged separately for high (red) and low (blue) SST – SAT days. The arrow shows the average SST in the area.

Figure 6. As in Figure 2a, but for (a) the differences in surface sensible heat flux (SHF) between the high and low SST – SAT days in NDJF2009 (ΔSHF); (b) Same as (a) but for the differences in surface latent heat flux (ΔLHF).

Figure 7. (a) As in Figure 1a, but for cloud liquid water path (CLWP). (b) As in Figure 2b, but for CLWP (ΔCLWP/CLWP). (c) Scatter plot between CLWP and SST – SAT based on all 0.75° × 0.75° data (non-precipitating water clouds) obtained in the Kuroshio study area in NDJF2009 (gray circles). Averages are also shown for all data (black line) and data only with CLWP > 80 g m^{-3} (red

line). (A few data points with CLWP > 300 g m^{-3} were removed before taking the averages). Vertical bars indicate standard deviations divided by the square root of the sample numbers, corresponding to standard deviations of estimated averages. The bars are generally very small and fall within the closed circles.

Figure 8. As in Figure 2a, but for the differences in lower-tropospheric stability (LTS) between the high and low SST – SAT days in NDJF2009 (ΔLTS). LTS is defined as the difference in potential temperature between 700 and 1000 hPa levels (θ_{700} - θ_{1000}).

Figure A1. Five-year winter climatology between 2008 and 2012 (NDJF 2008-2012). (a) – (c) As in Figures 2a, 2b, and 2e, respectively, but for NDJF 2008-2012 data; (d) As in Figure 4 but for NDJF 2008-2012 data.

Figure B1. (a) A slope of a regression line between N_c and SST–SAT ($dN_c/<N_c>)/d(SST–SAT)$) evaluated locally for individual 0.75° × 0.75° grid boxes using all daily data in NDJF2009 (non-precipitating water cloud). $<N_c>$ is the four-month average in individual grid boxes. (b) Same as (a) but for $[(dN_c/<N_c>)/d(SST–SAT)]$ Δ(SST–SAT). (c) Same as (a) but for (dAOD/<AOD>) /d(SST–SAT). (d) Same as (a) but for [(dAOD/<AOD>) /d(SST–SAT)] Δ(SST–SAT).

Table 1. Winter averages in the Kuroshio study area in 2009 [a]

	Average [b]	High SST-SAT days [c]	Low SST-SAT days [d]
τ	14.6 ± 10.8	17.5 ± 13.3	11.6 ± 7.98
r_e (μm)	7.44 ± 1.24	7.03 ± 1.31	7.82 ± 1.13
N_c (cm^{-3})	280 ± 119	335 ± 131	227 ± 88.9
CLWP ($g\ m^{-2}$)	62.8 ± 53.5	73.2 ± 65.2	51.8 ± 41.7
AOD	0.189 ± 0.122	0.201 ± 0.112	0.177 ± 0.13
SST (K)	296.24 ± 1.54	296.22 ± 1.63	296.20 ± 1.61
SAT (K)	291.22 ± 3.43	288.45 ± 3.24	293.83 ± 2.49
SST – SAT (K)	5.01 ± 2.88	7.77 ± 2.3	2.37 ± 1.75
SHF (Wm^{-2})	65.8 ± 55.6	117 ± 56.2	23.6 ± 23.3
LHF (Wm^{-2})	259 ± 145	372 ± 139	153 ± 89.2

[a] Kuroshio study area was defined in this study as a parallelogram shown in Figure 1 (23°N-26°N, 122°E and 28°N-31°N, 130°E). All quantities were evaluated using only daily 0.75° × 0.75° data obtained when non-precipitating water clouds were observed in January, February, November, and December 2009 (denoted by NDJF2009). Monthly averages were calculated before four-month averages were taken.

τ: cloud optical thickness, r_e: effective radius, N_c: cloud droplet number concentration, CLWP: cloud liquid water path, AOD: aerosol optical depth, SST: sea surface temperature, SAT: surface air temperature, SHF: sensible heat flux, and LHF: latent heat flux.

[b] Four-month averages.

[c] Averages for high SST – SAT days.

[d] Averages for low SST – SAT days.

Table 2. Winter averages of fractional changes between high and low SST – SAT days in the Kuroshio study area in 2009 [a]

Estimated parameters	Averages
$0.5\ \Delta\tau/\tau$ (%)	17.1
$-2.5\ \Delta r_e / r_e$ (%)	27.5
$\Delta N_c / N_c$ (%)	38.1
ΔCLWP /CLWP (%)	24.2
ΔAOD /AOD (%)	14.4

[a] As in Table 1, but for fractional changes of various parameters.

2016/9/20

Figure 1

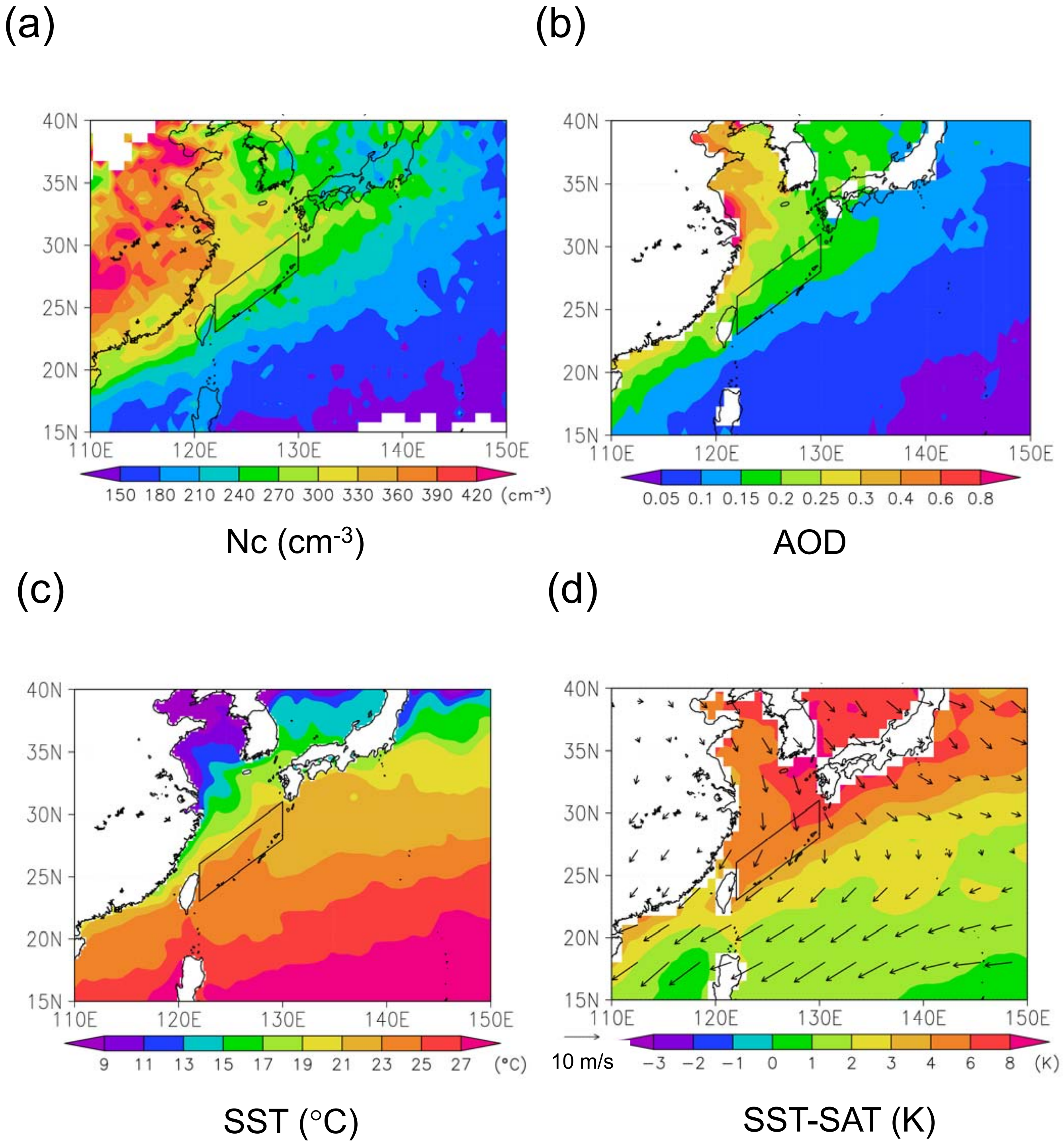

Figure 2

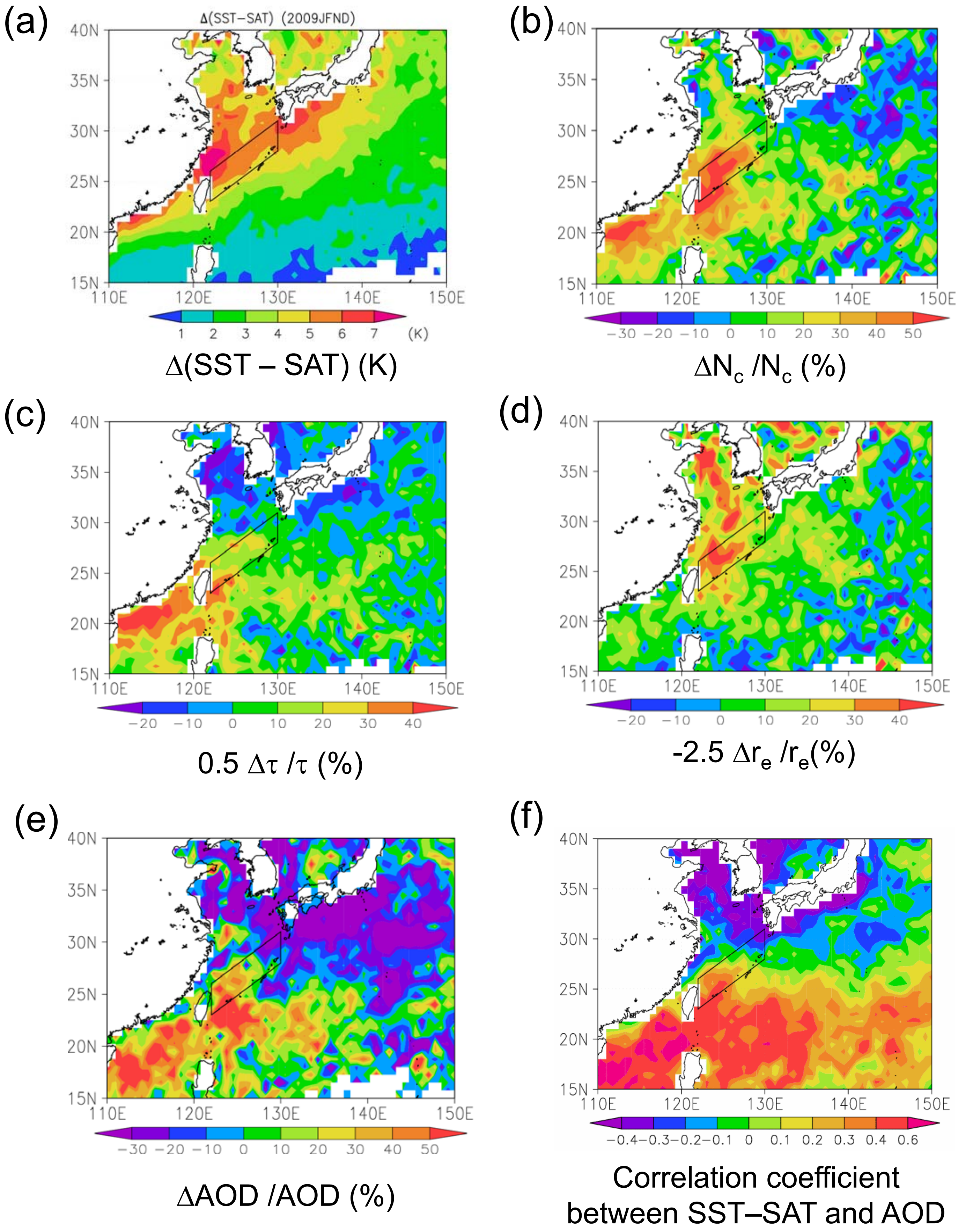
(a)
Δ(SST−SAT) (2009JFND)
40N
35N
30N
25N
20N
15N
110E 120E 130E 140E 150E
1 2 3 4 5 6 7 (K)
Δ(SST – SAT) (K)
(b)
−30 −20 −10 0 10 20 30 40 50
ΔNc /Nc (%)
(c)
−20 −10 0 10 20 30 40
0.5 Δτ /τ (%)
(d)
−20 −10 0 10 20 30 40
-2.5 Δre /re(%)
(e)
−30 −20 −10 0 10 20 30 40 50
ΔAOD /AOD (%)
(f)
−0.4 −0.3 −0.2 −0.1 0 0.1 0.2 0.3 0.4 0.6
Correlation coefficient
between SST–SAT and AOD

Figure 3

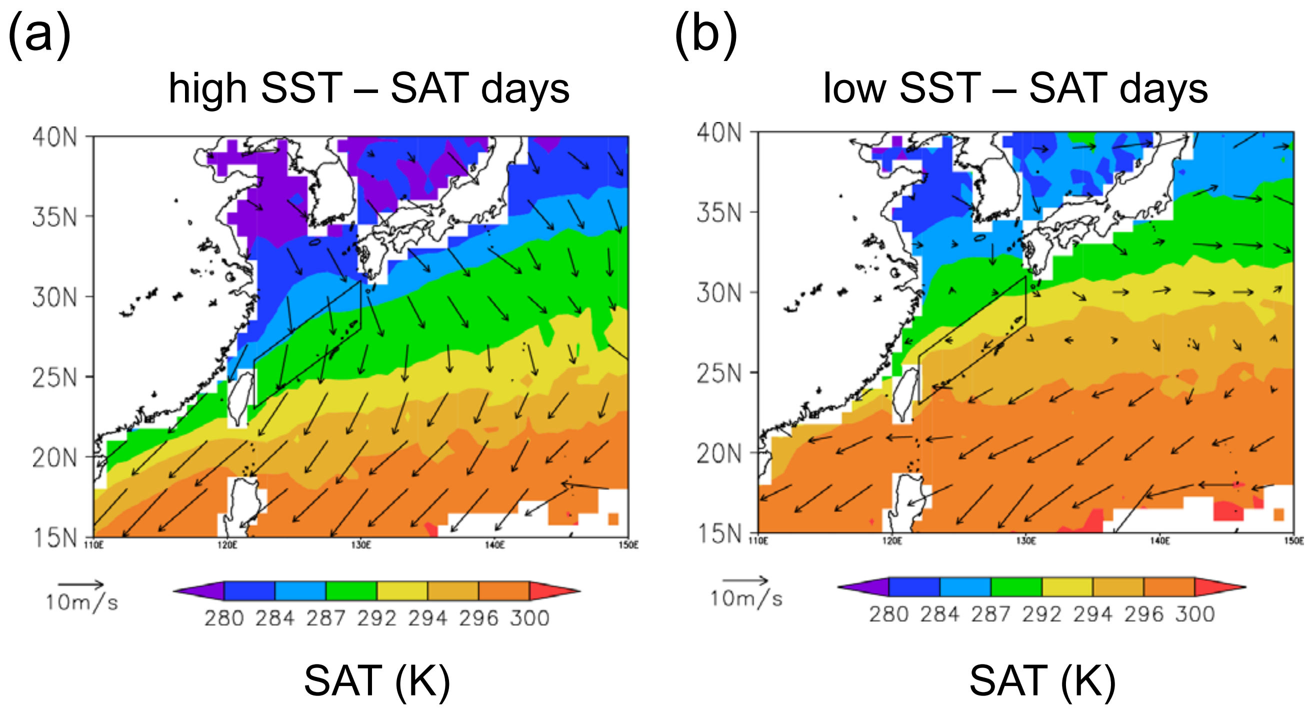

(a)
high SST – SAT days
40N
35N
30N
25N
20N
15N
110E
120E
130E
140E
150E
10m/s
280 284 287 292 294 296 300
SAT (K)
(b)
low SST – SAT days
40N
35N
30N
25N
20N
15N
110E
120E
130E
140E
150E
10m/s
280 284 287 292 294 296 300
SAT (K)

Figure 4

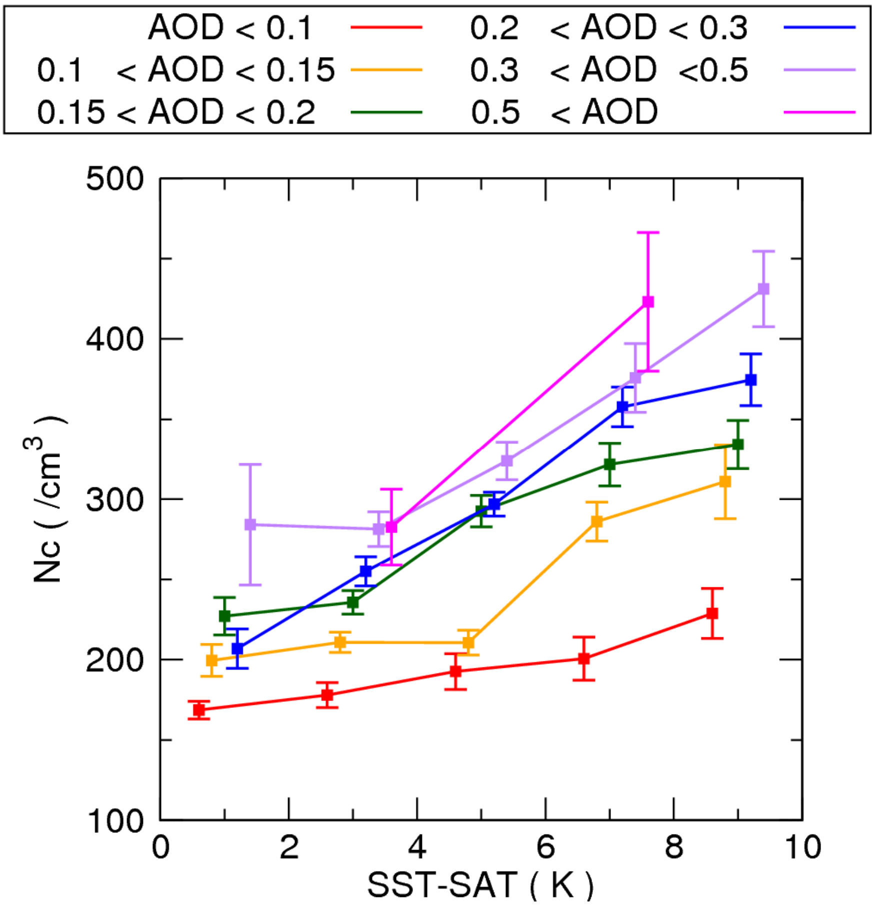

AOD < 0.1
0.1 < AOD < 0.15
0.15 < AOD < 0.2
0.2 < AOD < 0.3
0.3 < AOD <0.5
0.5 < AOD
Nc (/cm^3)
SST-SAT (K)
500
400
300
200
100
0
2
4
6
8
10

Figure 5

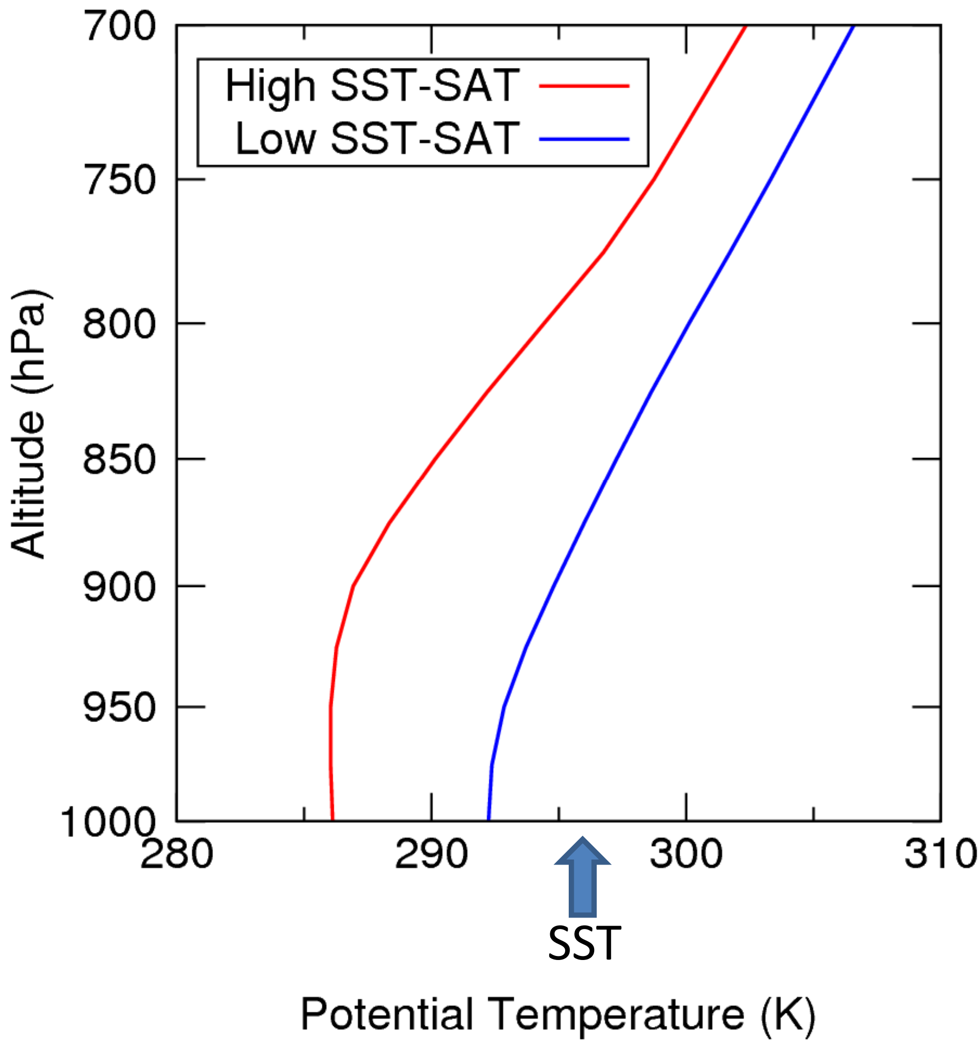

700
750
800
850
900
950
1000
Altitude (hPa)
High SST-SAT
Low SST-SAT
280
290
300
310
SST
Potential Temperature (K)

Figure 6

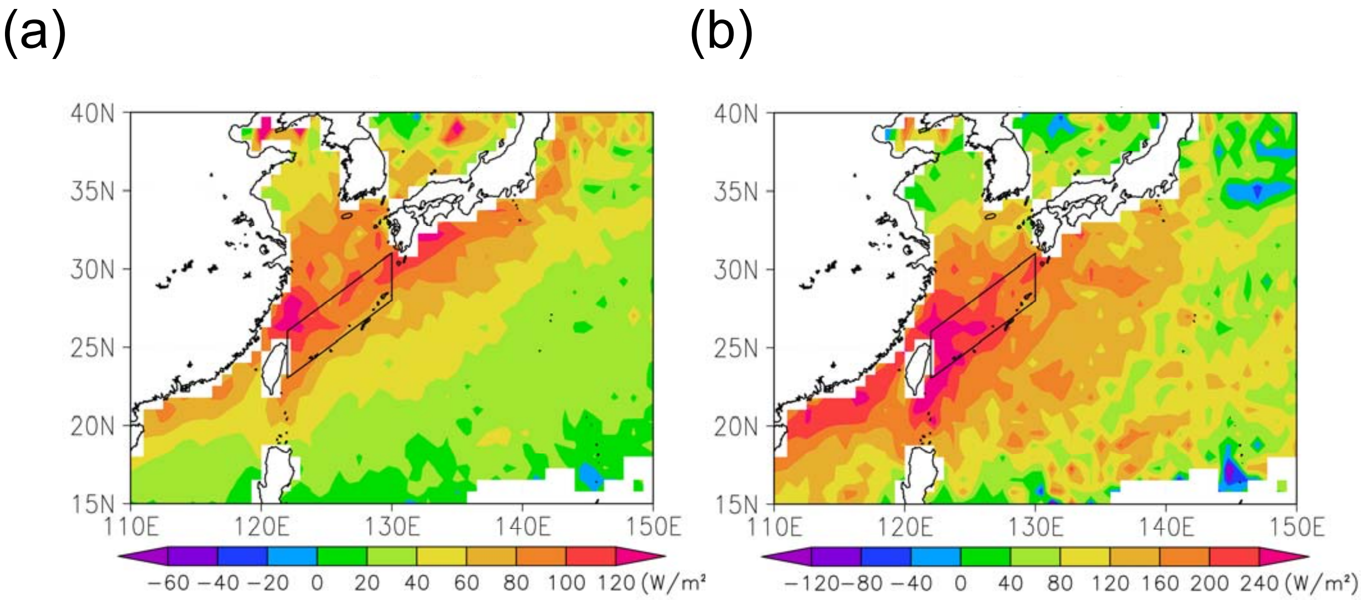

ΔSHF (W m^{-2})   ΔLHF (W m^{-2})

Figure 7

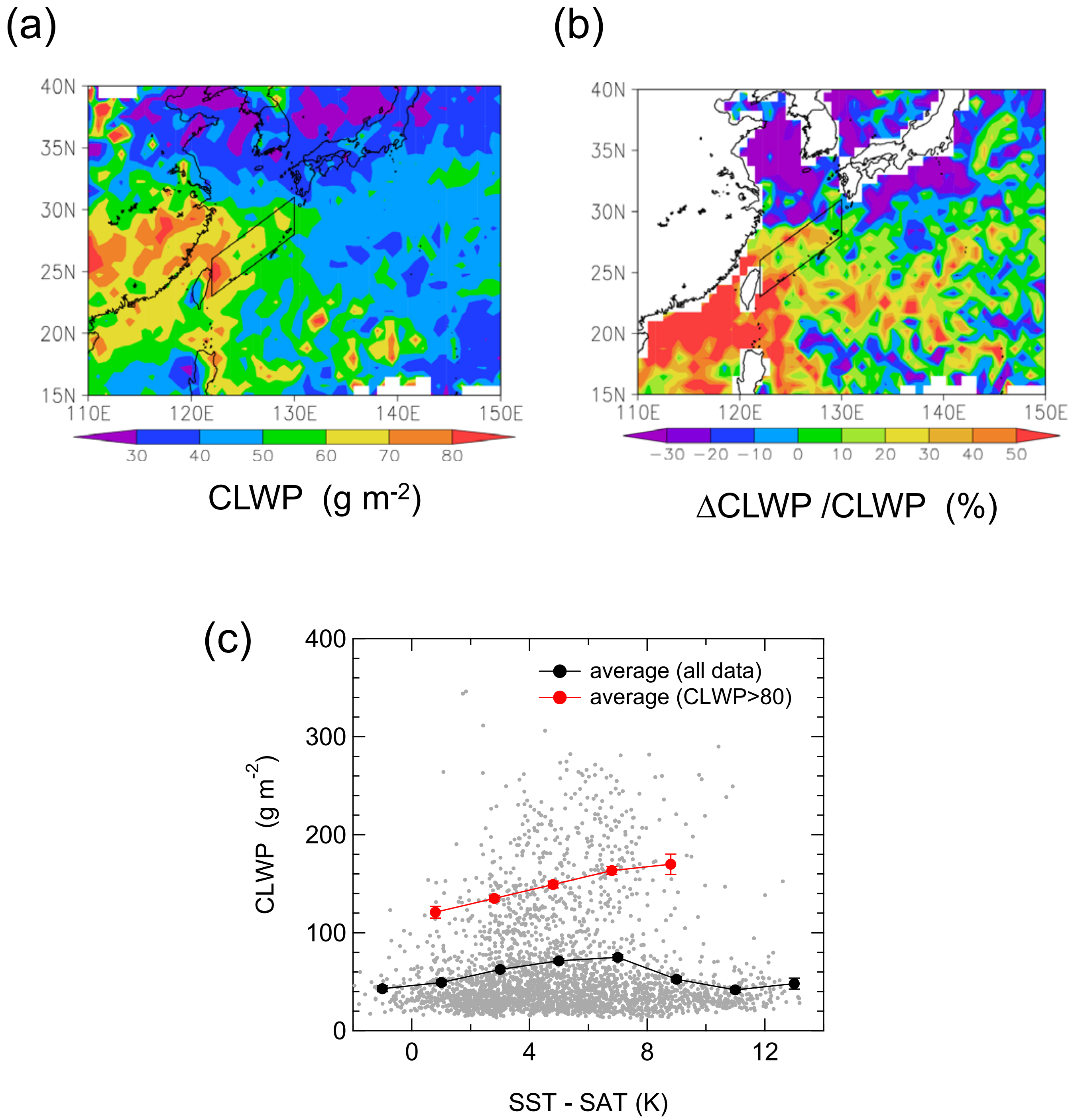

(a)
(b)
40N
35N
30N
25N
20N
15N
110E
120E
130E
140E
150E
30
40
50
60
70
80
CLWP (g m-2)
−30 −20 −10 0 10 20 30 40 50
ΔCLWP /CLWP (%)
(c)
400
300
200
100
0
CLWP (g m-2)
average (all data)
average (CLWP>80)
0
4
8
12
SST - SAT (K)

Figure 8

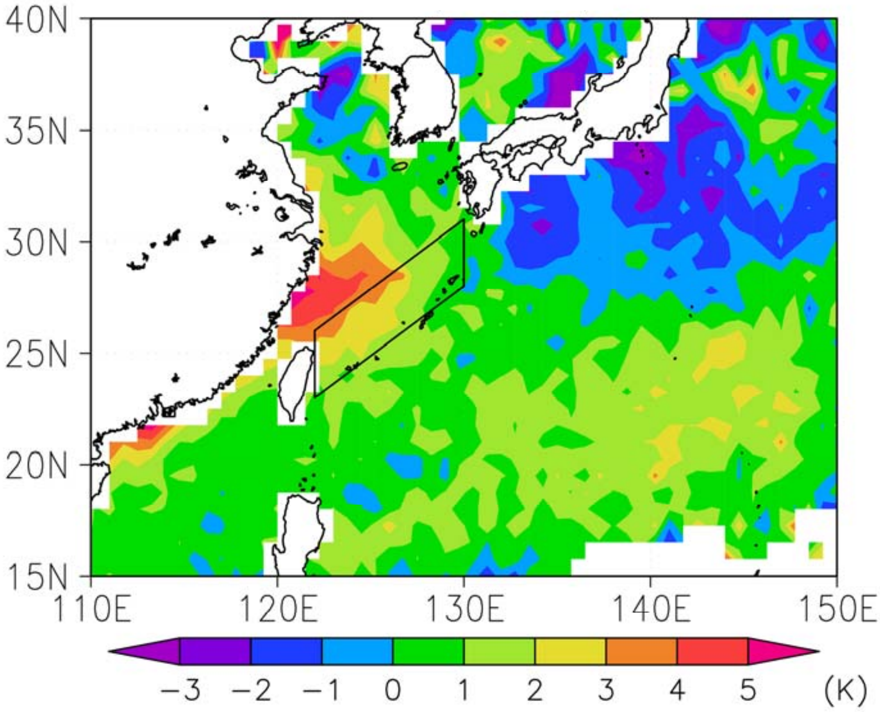

ΔLTS (K)

Figure A1

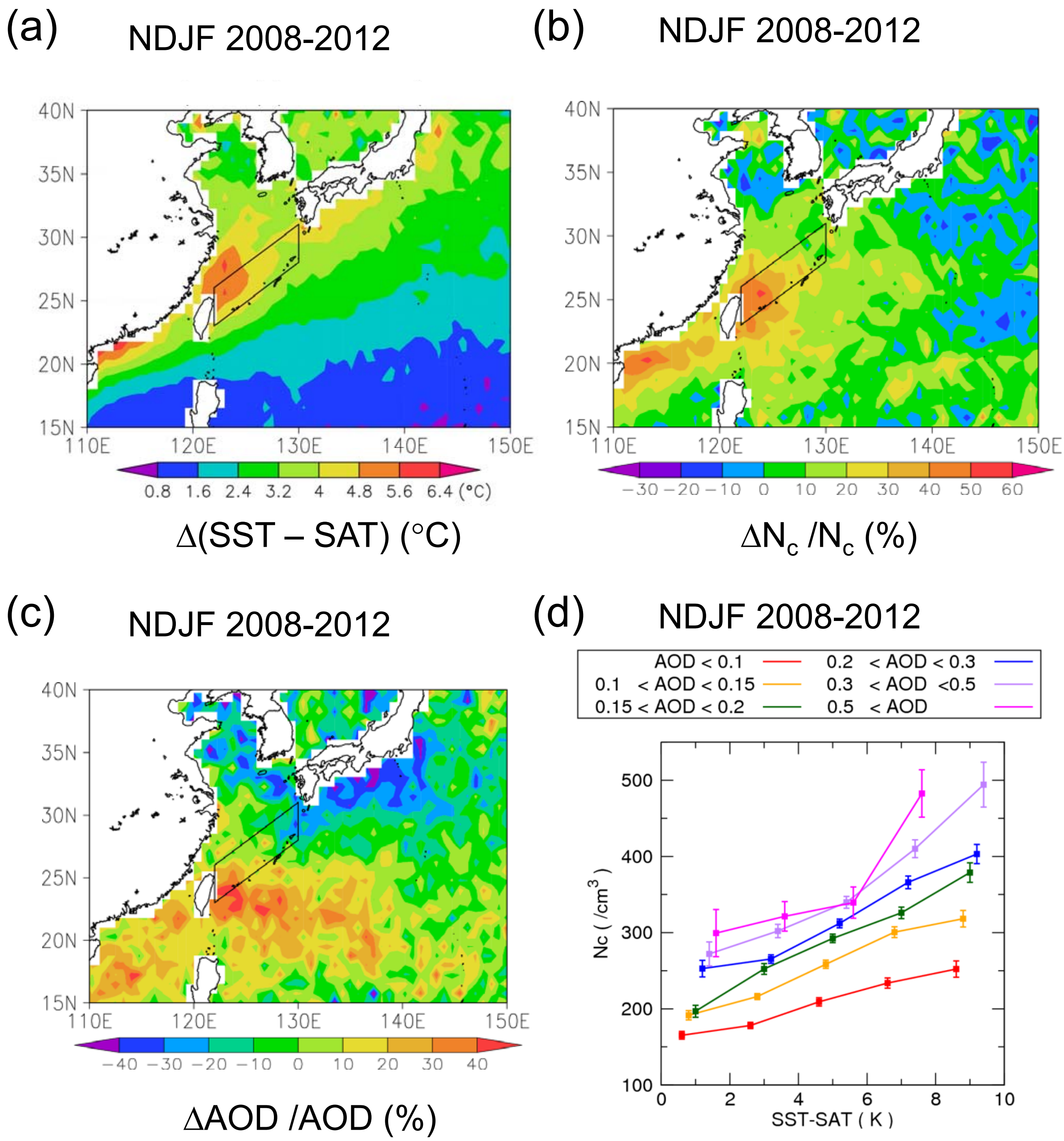
(a)
NDJF 2008-2012
40N
35N
30N
25N
20N
15N
110E
120E
130E
140E
150E
0.8 1.6 2.4 3.2 4 4.8 5.6 6.4 (°C)
Δ(SST – SAT) (°C)
(b)
NDJF 2008-2012
−30 −20 −10 0 10 20 30 40 50 60
$\Delta N_c / N_c$ (%)
(c)
NDJF 2008-2012
−40 −30 −20 −10 0 10 20 30 40
ΔAOD /AOD (%)
(d)
NDJF 2008-2012
AOD < 0.1
0.1 < AOD < 0.15
0.15 < AOD < 0.2
0.2 < AOD < 0.3
0.3 < AOD <0.5
0.5 < AOD
Nc (/cm^3)
100
200
300
400
500
0
2
4
6
8
10
SST-SAT (K)

Figure B1

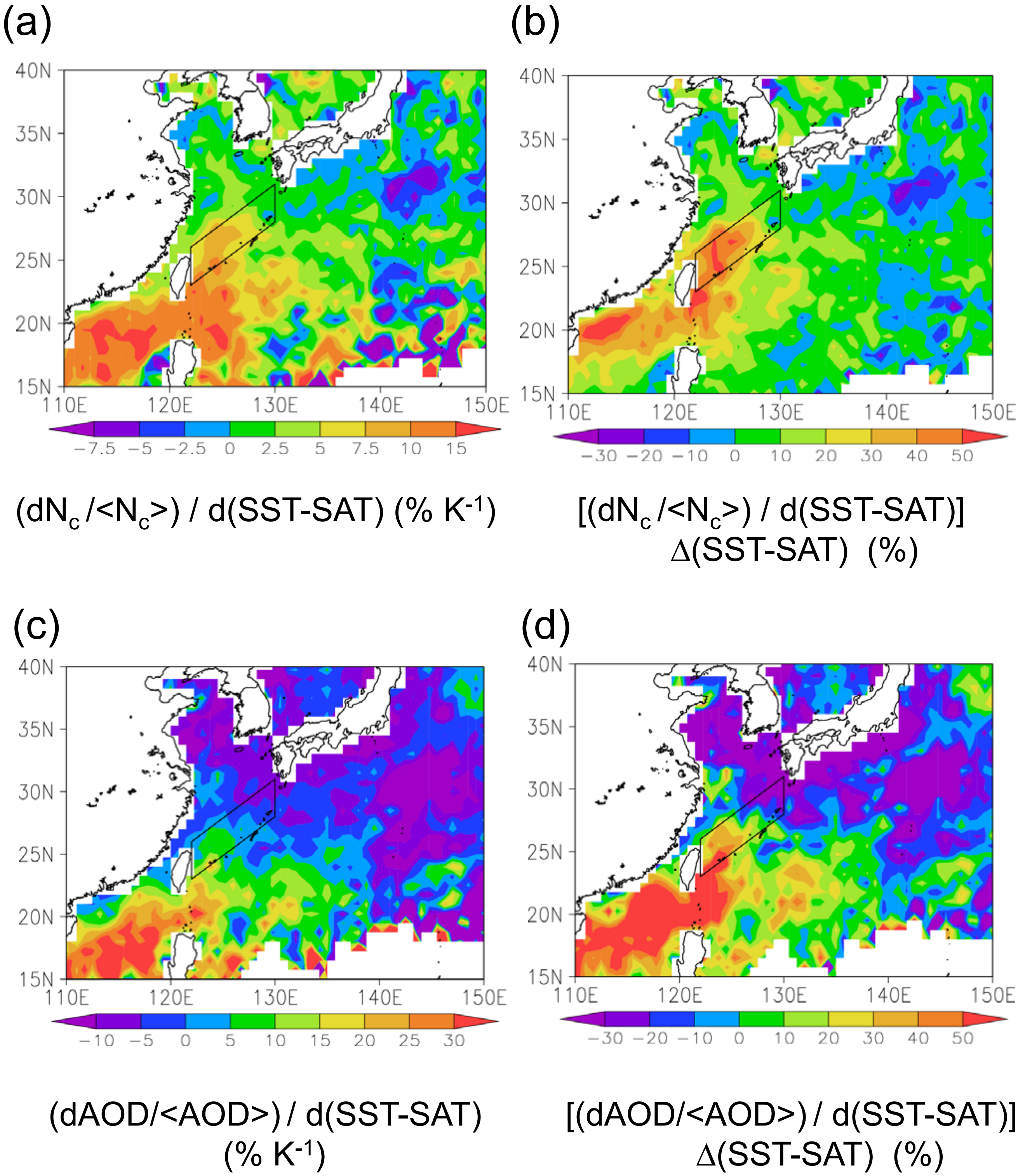
(a)
40N 35N 30N 25N 20N 15N
110E 120E 130E 140E 150E
−7.5 −5 −2.5 0 2.5 5 7.5 10 15
$(dN_c/\langle N_c\rangle)$ / d(SST-SAT) (% K^{-1})
(b)
40N 35N 30N 25N 20N 15N
110E 120E 130E 140E 150E
−30 −20 −10 0 10 20 30 40 50
$[(dN_c/\langle N_c\rangle)$ / d(SST-SAT)]
Δ(SST-SAT) (%)
(c)
40N 35N 30N 25N 20N 15N
110E 120E 130E 140E 150E
−10 −5 0 5 10 15 20 25 30
(dAOD/<AOD>) / d(SST-SAT)
(% K^{-1})
(d)
40N 35N 30N 25N 20N 15N
110E 120E 130E 140E 150E
−30 −20 −10 0 10 20 30 40 50
[(dAOD/<AOD>) / d(SST-SAT)]
Δ(SST-SAT) (%)